CIMAC CONGRESS 25
ZURICH, MAY 19 – 23, 2025

2025 | 188

Modelling of in-cylinder processes of large, two-stroke LGI engines using an integrated CFD-FEM tool

Fuel Injection & Gas Admission and Engine Components

Kar Mun Pang, MAN Energy Solutions

Nicolai Arent Quist, MAN Energy Solutions
Nikolaj Hovmøller, MAN Energy Solutions
Jiun Cai Ong, MAN Energy Solutions
Simon Matlok, MAN Energy Solutions
Thomas Schaldemose Norman, MAN Energy Solutions
Stefan Mayer, MAN Energy Solutions

ABSTRACT

In our previous work, we presented the chemistry coordinate mapping (CCM) clustering method to increase the efficiency in the direct integration of chemical kinetic mechanisms for dual-fuel combustion in two-stroke, low-speed marine liquid gas injection (LGI) engines. The former work used LGI methanol (LGIM) experimental data from the 50cm bore, two-stroke research test engine at MAN Energy Solutions in Copenhagen, Denmark, for model evaluation. The parallel efficiency of the CCM solver was recently improved. The new CCM solver is named CCM Point-to-Point Communication (CCM-P2P). In this work, the former 50cm bore LGIM engine simulations are revisited. The LGIM simulations show that a threefold speed-up is achieved compared with the former CCM version. In addition, the CCM-P2P solver is applied to simulate a 50cm bore LGI ammonia (LGIA) engine. With additional consideration of principal variables, the CCM-P2P solver reproduces results from the direct integration (without the clustering method) reasonably well. A speed-up may reach up to 75%, depending on the chemical mechanism size. Such speed-up allows the implementation of more comprehensive chemical mechanisms to gain more insights of the in-cylinder processes and facilitate evaluation of the performance of different chemical mechanisms. The current study also found that the semi-global approach (SGA) models perform reasonably well at predicting in-cylinder combustion and emission characteristics compared with their skeletal counterparts in both the 50cm bore LGIM and LGIA engine simulations. Further appraisal is made in terms of predicting the heat transfer to different engine components during the engine combustion phase for a 95cm bore LGIM engine and a 60cm bore LGIA engine. The SGA models are able to reproduce the temporal evolution of heat transfers to different engine components, including heat transfers to the external walls of fuel injectors. In the subsequent part of the paper, we present our integrated CFD-FEM toolbox for the estimation of the external injector wall temperature. To perform a fair comparison with the temperature measurement, using solely the CFD engine combustion simulation is not sufficient. CFD in-nozzle simulation and scavenging flow simulations are hence performed, and multiple sets of CFD results are provided for the FEM analysis. The model evaluation is carried out for the 95cm bore LGIM engine. Two operating modes, i.e., diesel mode and methanol mode are simulated. The full cycle in-cylinder pressure predicted by the current CFD model is compared with the measurement from the engine shop test. A comparison of the integrated CFD-FEM results with the external injector wall temperature measurements shows that the current model is capable of replicating the measurements reasonably well. The CFD-FEM toolbox is able to predict the change of temperature with respect to measurement positions and operating modes correctly. Compared with the measurement, the maximum percentage difference is approximately 6% for all the simulation results, apart from those for the back outer position in the LGIM mode, which is approximately 13%. Once further validated, the CFD-FEM toolbox will be useful for injector layout.

1 INTRODUCTION

Maritime transportation is an essential element of the transportation sector and constitutes a major part of worldwide trade. This situation is expected to continue in the foreseeable future, and decarbonisation of the maritime industry is hence inevitable. In the last couple of years, MAN Energy Solutions, the leading provider of marine main propulsion engines, has put marine two-stroke engines operating on liquefied petroleum gas (LPG), liquefied natural gas (LNG), ethane, and methanol into operation. Furthermore, MAN Energy Solutions is currently developing engines operating on ammonia [1].

Depending on the engine bore size, each cylinder in MAN B&W gas injection (GI), and liquid gas injection (LGI) dual-fuel two-stroke engines is equipped with two to three liquid fuel injectors for fuel oil and two to three fuel injectors for alternative fuels. In dual-fuel modes, the fuel oil injectors deliver pilot fuels for igniting the alternative fuels, which commonly have high autoignition temperatures. Ignition timing, ignition location, and jet flame development of the pilot fuel are crucial for efficiently burning the succeeding alternative fuels delivered during the main injection. In conventional diesel mode, only fuel oil is delivered for full operation. The layout of these injectors is crucial for engine performance in terms of high combustion efficiency and low emission levels.

Another important aspect is heat transfer in the engine, which in turn influences the indicated efficiency. A more detailed understanding of in-cylinder processes is therefore important to minimise the overall fuel consumption and maximise the benefits of implementing these alternative fuels. Besides that, extending the lifespan of engine components, such as the fuel nozzle, is also a crucial step to ensure the continuous and more widespread use of alternative fuels. Cooling occurs on the inner surface of the fuel nozzle and is more substantial when liquid fuels with high latent heat of vaporisation and low viscosity, such as methanol and ammonia, are used. Meanwhile, the outer surface of the fuel nozzle is exposed to heat due to neighbouring jet flames. The cooling and heating processes within an engine cycle may lead to thermal fatigue on the fuel nozzles.

The coupling of chemical kinetic mechanism with three-dimensional (3D) computational fluid dynamics (CFD) models is useful for understanding in-cylinder processes and supporting the injector layout. Conventionally, CFD dual-fuel combustion modelling is carried out using a skeletal diesel surrogate mechanism, such as *n*-heptane chemistry, which also consists of the chemical reactions for alternative fuel oxidation. However, such a skeletal model typically consists of a large number of species, ranging from 50 to 200 for dual-fuel combustion of *n*-heptane/methanol and *n*-heptane /ammonia.

To achieve a balance between computational efficiency and accuracy in 3D CFD simulations of dual-fuel combustion in large two-stroke marine engines, a previous study presented a semi-global approach (SGA), where a global *n*-heptane mechanism was combined with a reduced methanol model [2]. The model's performance was compared to that of a skeletal *n*-heptane mechanism in a two-stroke engine operating on methanol. The assumptions made in the formulation of the SGA were systematically analysed. Pang et al. [2] also presented the implementation of a clustering method, namely chemistry coordinate mapping (CCM) for these simulations, where both pilot and main fuels burn in a non-premixed manner. CCM is a method designed to improve the efficiency of combustion simulations by grouping similar cells based on their thermochemical states. In this approach, multiple cells sharing similar thermochemical states can use the same set of reaction rates, reducing the overall computational workload by avoiding redundant calculations across cells with nearly identical chemical behaviours [3].

In-cylinder pressure, heat release rate (HRR), and species profiles collectively showed that the former CCM solver could replicate the direct integration results i.e. without using the CCM solver, and the computational runtime was reduced by approximately 80%. Yet, there is a room for further improvement. In the conventional CCM method, the workloads among computational cores during parallel simulations are imbalanced. Some cores handle cells or regions filled with pure air where no reaction happens, requiring minimal computational effort, while others are burdened with cells undergoing complex combustion processes. These disparities necessitate a more effective load balancing strategy to distribute computational workloads evenly. Load balancing in a conventional CCM employs a gathering and scattering method. In this method, all cores first send their data to a central master core (gathering), which then processes the data and redistributes it back to the respective cores (scattering). This centralised approach, while straightforward, creates bottlenecks that limit the efficiency and scalability in large-scale computations. Chemistry Coordinate Mapping with Point-to-Point communication (CCM-P2P) has been developed to overcome these limitations It introduces a more efficient communication strategy that bypasses the master core and enables direct data exchange between

cores. This efficient speed-up tool allows for the screening of more comprehensive combustion chemistry under realistic large-bore two-stroke marine engine conditions within a reasonable timeframe. Evaluating the chemistry scheme is crucial prior to studying the in-cylinder combustion, emission formation, and heat transfer phenomena to ensure the reliability of the simulation results.

Set against this background, this paper first reports the implementation of the CCM-P2P solver for 3D CFD modelling of dual-fuel combustion in two-stroke, low-speed marine LGI engines operating on methanol and ammonia. The CCM-P2P is used to efficiently appraise the performance of different chemistry schemes in terms of combustion and emission predictions. Further assessment is subsequently performed from a heat transfer perspective. The last section of this paper presents the coupled CFD-FEM toolbox for the estimation of injector wall temperature. Each section provides a numerical formulation as well as descriptions of the engine specifications and operating conditions.

2 SPEED-UP TOOL FOR EVALUATION OF CHEMICAL MECHANISMS

2.1 Numerical formulation

The 3D CFD simulations are carried out using the open-source code, OpenFOAM [4]. The fuel spray, flow, and combustion processes are modelled using a Lagrangian-Eulerian approach. Unsteady Reynolds averaged Navier-Stokes (URANS) simulations are performed for turbulence modelling. The description of mesh configuration and sub-models can be found in the former work [2]. Here, only the tested chemical mechanisms and the CCM-P2P setup are described.

2.1.1 Dual-fuel chemical kinetic mechanisms

The SGA concept is based on the following two assumptions: (1) the interaction between pilot and main fuel combustion is mainly due to the high gas temperature from the pilot fuel combustion rather than the intermediate radicals from the pilot fuel combustion, and (2) soot formation is negligible in the pilot fuel combustion due to the small amount of fuel used, and the main fuel combustion of ammonia or methanol due to the absence of C-C chemical bonds in these fuels. In the SGA formulation, *n*-heptane (C_7H_{16}) is used as a diesel surrogate, and the associated oxidation is modelled by using a four-step global scheme from Müller et al. [5]. Thorsen et al. [6] formulated the global scheme in CHEMKIN format [7] and evaluated it under large two-stroke marine engine-like conditions.

2.1.1.1 *n*-Heptane/methanol

The SGA model for *n*-heptane/methanol oxidation is adopted from [2], where the four-step global scheme is integrated with the skeletal methanol oxidation mechanism. It consists of 22 species and 96 reactions. This chemical kinetic model is henceforth named the SGA-M22 mechanism. A 68-species mechanism developed by Lu and Law [8] is combined with NO_X reactions to form a skeletal mechanism with 72 species. This chemical kinetic model is henceforth referred to as the SK-M72 mechanism.

2.1.1.2 *n*-Heptane/ammonia

Alekseev and Nilsson [9] developed a base *n*-heptane/ammonia mechanism, comprising 143 species and 989 reactions, following the approach of Wang et al. [10]. The *n*-heptane sub-mechanism in [10] was a modified version of the reduced model of Chang et al. [11]. It was merged with the detailed H/N/O and the C/H/N/O sub-mechanisms of Thorsen et al. [12], while keeping the hydrogen sub-mechanism from [12]. The C_3-C_7 interaction subset was based on [12]. Reaction rates for the same classes as in [12] were reconstructed for C_3-C_7 in [10]. Alekseev and Nilsson [9] subsequently developed a reduced version, where the ant-colony reduction methodology [13] has been utilised, combined with differential evolution optimisation [13] and a sequence of manual steps. The resulting reduced mechanism contains 57 species and 159 reactions and is henceforth named SK-A57. It was found that in the considered target space, the present mechanism performs as good as the larger models. Co-oxidation of *n*-heptane and ammonia is considered in this mechanism. In the present work, the ammonia oxidation reactions are extracted from the SK-A57 mechanism and combined with the four-step global *n*-heptane scheme. The resulting mechanism consists of 28 species with 71 reactions and is henceforth known as SGA-A28. The third mechanism tested here is the SGA-A33 model. Similar to the SGA-A28, the four-step global *n*-heptane model is combined with the detailed ammonia oxidation mechanism adopted from Stagni et al. [14]. This mechanism comprises 33 species and 206 reactions.

2.1.2 Chemistry Coordinate Mapping with Point-to-Point Communication

To reduce communication overhead and improve scalability in parallel computations, CCM-P2P was developed at Lund University. CCM-P2P employs a round-robin algorithm to optimise core-to-core communication during load balancing. By leveraging the round-robin communication model, CCM-P2P achieves direct core communication, improved scalability, reduced bottlenecks, and enhanced efficiency. The standard resolutions of

the thermodynamic space of (T, ξ, $e^{(-\chi)}$, Y_{pilot}, Y_{main}) are fixed at 5 K, 0.01, 0.025, 0.001, 0.001, respectively [2], where T is the gas temperature, ξ is the Bilger mixture fraction, and χ is an analogy of the scalar dissipation rate ranging from 0 to 1. Y represents the fuel mass fraction of evaporating species from pilot and main injections, respectively.

2.2 Results and discussions

Two 100% engine load test cases are used to illustrate the performance of the CCM-P2P solver. The simulated dual-fuel engine is the 4T50ME-X research engine at MAN Energy Solutions. The test engine has four cylinders with a bore of 50 cm and a stroke of 220 cm. At full load, the test engine produces 7 MW power at an engine speed of 123 rev/min. The engine is of the uniflow-scavenged type, with scavenge air intake ports at the bottom of each cylinder and a centrally located exhaust valve at the top. The in-cylinder flow is defined by a strong swirling motion introduced with the scavenge air. In the standard configuration, each cylinder is equipped with two liquid fuel injectors for fuel oil. One cylinder was modified to operate on methanol or ammonia. Methanol and ammonia operating modes are henceforth addressed as LGIM and LGIA, respectively. Two additional liquid fuel injectors were installed to supply methanol or ammonia fuel to the modified cylinder. The liquid injectors for fuel oil are used to deliver pilot fuels for igniting the methanol or ammonia. More information can be found in [2].

2.2.1 LGI Methanol

This section revisits the LGIM simulations from the previous work [2]. The specific objective here is to compare the performance of the previous CCM and the newly developed CCM-P2P in terms of computational efficiency. Different configurations of chemistry solvers and chemical kinetic mechanisms are listed in Table 1.

Table 1. Tested numerical configuration in LGIM simulations.

Setup	Chemistry solver	Chemical mechanism
I	Direct integration	SK-M72
II	CCM	SK-M72
III	CCM-P2P	SK-M72
IV	CCM-P2P	SGA-M22

Comparisons between simulated in-cylinder pressure and HRR using direct integration (DI), CCM and CCM-P2P for the LGIM mode are carried out, where the SK-M72 mechanism is used. Similar to previous findings, the calculated maximum pressure for the CCM case matches that of the DI case, with a negligible discrepancy of less than 1.0% (not shown).

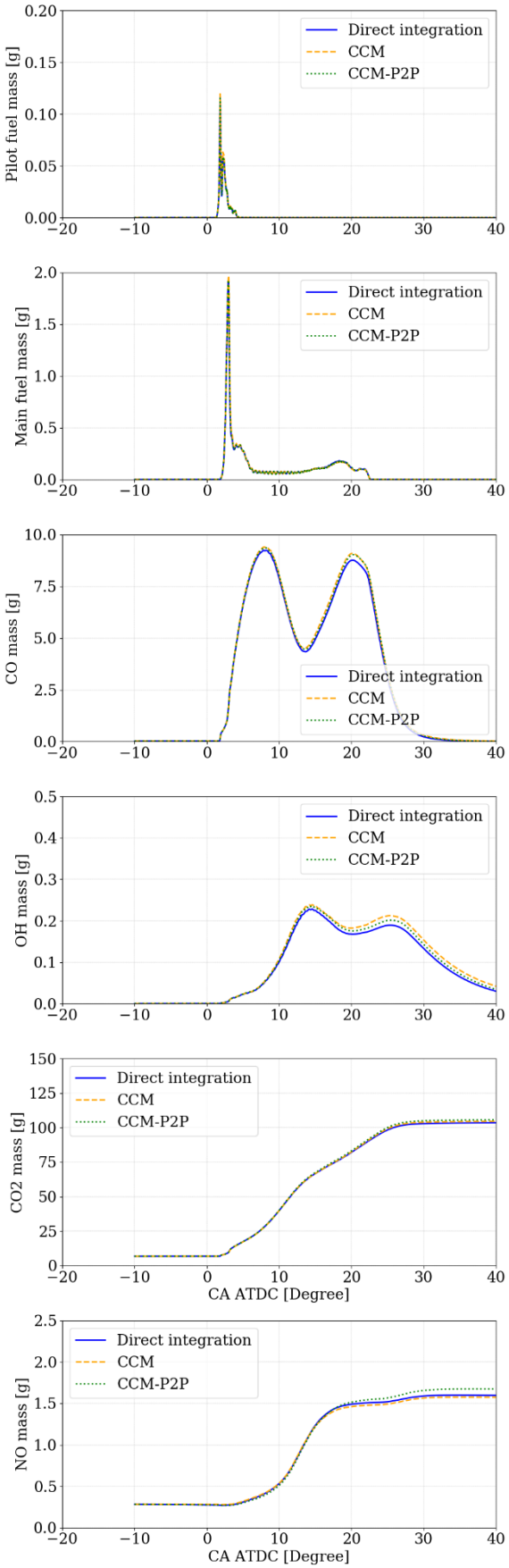

Figure 1. Comparisons of the temporal evolution of selected species, calculated with the DI, CCM and CCM-P2P solvers.

Temporal onset and the consequent evolution of selected species are next then compared to those generated using DI in Figure 1. Three fuel-rich species, pilot fuel (C_7H_{16}), main fuel (CH_3OH) and CO, predicted by both solvers are comparable. Similar trends can also be seen for the formation of important species near diffusion flame regions, *i.e.*, hydroxyl radical (OH), CO_2, and NO. The pressure, HRR, and species profiles collectively show that the CCM-P2P solver can replicate the DI and former CCM results.

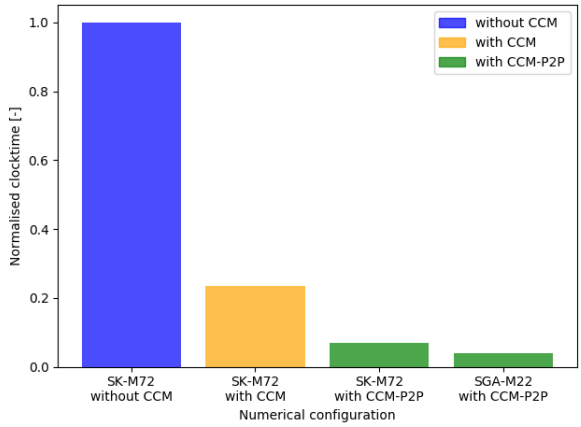

Figure 2. Comparisons of normalised clock time using the DI, CCM and CCM-P2P solvers.

Figure 2 demonstrates the normalised clock time of the four CFD setups with different configurations. The clock time is normalised by the clock time used by SK-M72 without CCM (DI). A reduction of approximately 80% was achieved with the former version of CCM as compared to DI when SK-M72 was applied. With the implementation of the CCM-P2P solver, a speed-up of more than 3-fold is achieved. The clock time drops by approximately 50% with the use of the SGA-M22 model without losing the accuracy of main combustion characteristics (*cf.* [2]). Figure 3 depicts that SGA-M22 is able to reproduce the in-cylinder averaged temperature as that of the skeletal counterpart, implying the reliability for heat transfer simulations.

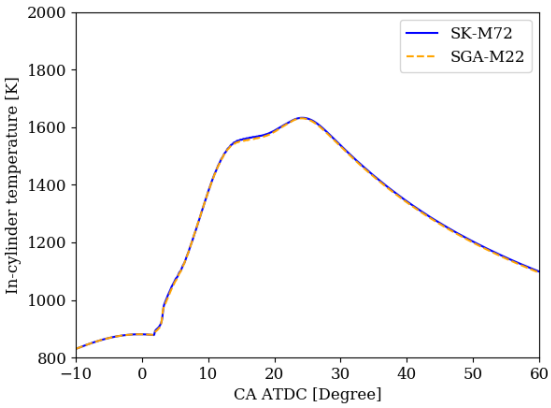

Figure 3. Comparison of in-cylinder average temperature using the SK-M72 and SGA-M22.

2.2.2 LGI Ammonia

This section evaluates the performance of CCM-P2P in the LGIA engine simulation. In the selected case, the initial pressure and temperature are set to 124 bar and 925 K, respectively. Results generated by different configurations of chemistry solvers and chemical models are shown in Table 2.

Table 2. Test numerical configurations in LGIA simulations.

Setup	Chemistry solver	Chemical mechanism	CCM-P2P principle variables
I	Direct integration	SK-A57	-
II	CCM	SK-A57	Standard [2]
III	CCM-P2P	SK-A57	With NO and N_2O
IV	CCM-P2P	SGA-A28	With NO and N_2O
V	CCM-P2P	SGA-A33	With NO and N_2O

2.2.2.1 Comparison between standard and customised CCM-P2P configurations

Comparisons of simulated in-cylinder combustion characteristics using both DI and CCM-P2P are carried out. The SK-A57 model is used in these comparisons. The calculated pressure for CCM-P2P with different principle variables (PVs) agrees well with that of the DI solver (see Figure 4).

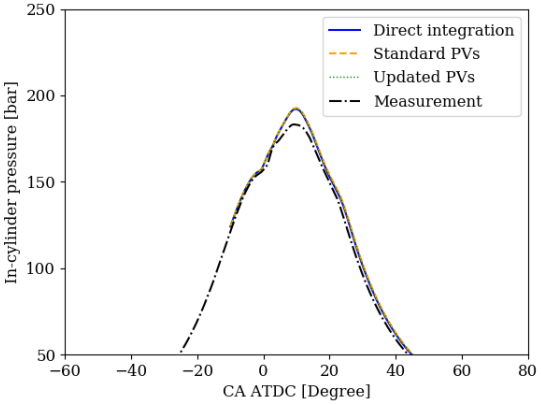

Figure 4. Comparisons of measurement and pressure profiles calculated using different models.

The temporal evolution of selected species is compared to those generated using DI in Figure 5. Predictions of three fuel rich species, pilot fuel (C_7H_{16}), main fuel (NH_3) and NH_2, are comparable for all chemistry solvers. Similar trends can also be seen for the hydroxyl radical (OH). However, N_2O prediction shows a more apparent discrepancy when the standard CCM-P2P configuration is used. Such discrepancy reduces when additional PVs of NO and N_2O are considered. Figure 6 demonstrates that additional PVs result in a higher number of CCM phase-space cells.

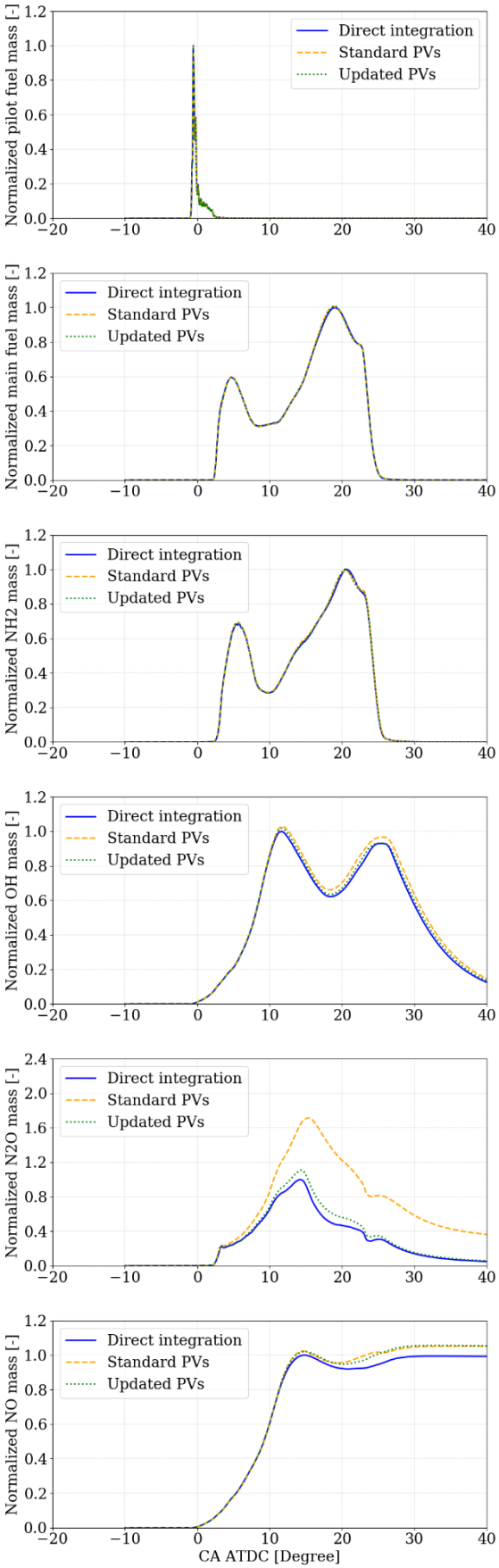

Figure 5. Comparisons of the temporal evolution of selected species, calculated using DI and CCM-P2P with standard and updated PVs.

Current results show that the CCM-P2P solver with updated PVs can replicate the DI results, with a computational runtime reduction of approximately 75%. It may be worth mentioning that the speed-up gained in the LGIA simulation is lower than that in the LGIM simulation. This is mainly due to the more complex ammonia chemistry, which results in a higher number of CCM phase-space cells. A comparison of CCM phase-space cells in the current LGIM and LGIA cases can be found in Figure 6.

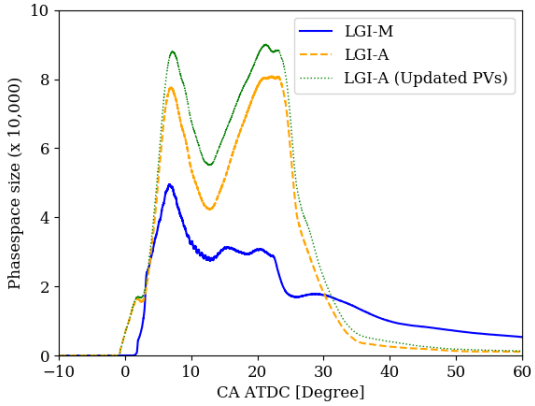

Figure 6. Comparisons of CCM phase-space size for different cases.

2.2.2.2 Comparison of *n*-heptane/ammonia mechanisms

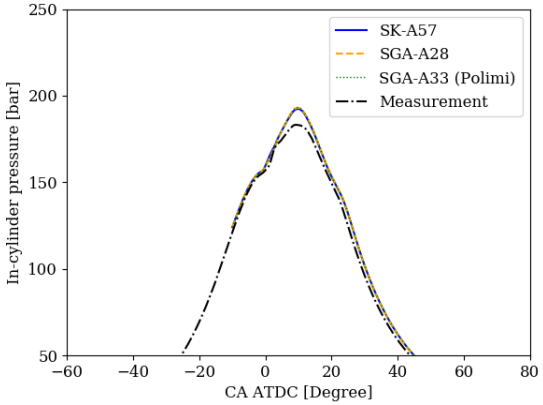

Figure 7. Comparisons of measured and calculated pressure profiles using different models.

This section evaluates the concept of SGA for LGIA application, which was not considered in the former work [2]. The updated PV configuration is applied here. As shown in Figure 7, the pressure profiles predicted by various chemical models closely resemble the measurements , with a maximum difference of 5% for the peak value. Similar to the observations in the LGIM simulation, the SGA models predict a lower pilot fuel oxidation rate as compared to the SK-A57 mechanism. This can be seen in Figure 8 and is expected due to the two different *n*-heptane oxidation reactions.

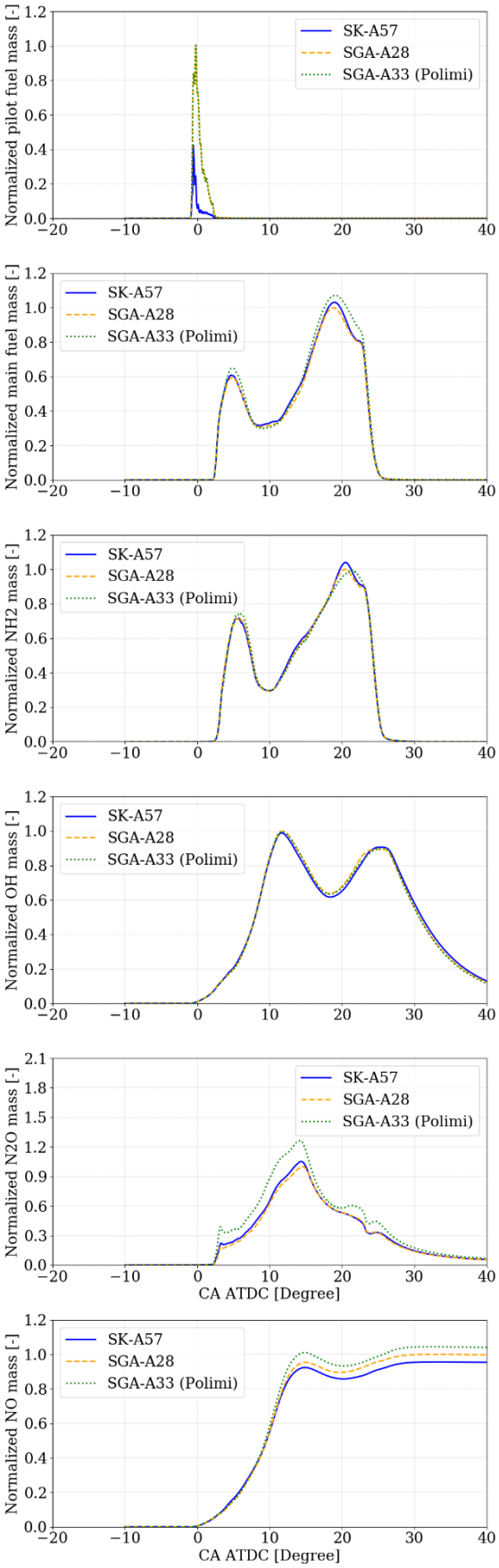

Figure 8. Comparisons of temporal evolution of selected species, calculated using different chemistry schemes.

Comparing SK-A57 and SGA-A28, which have the same NH_3 oxidation chemistry, the evolutions of main radicals and emissions are all comparable. For example, a similar trend is observed for the initial phase of NH_3 oxidation. It is noted that the simulated gaseous-phase NH_3 peaks again after 10 CAD ATDC. This trend is well replicated by the SGA models as well. It is worth mentioning that, due to the small amount of pilot fuel, the net production of OH is rather low during the pilot fuel combustion (*cf.* Figure 8). This indicates that the interaction between pilot and main fuel combustion is mainly caused by the high gas temperature from pilot fuel combustion, and not the intermediate radicals from the pilot fuel combustion in the LGIA engine.

During the main combustion and post-oxidation phases, the evolutions of NH_2 and OH predicted by both models are identical. Figure 8 also demonstrates a high degree of agreement between temporal evolutions of N_2O and NO masses predicted by SK-A57 and SGA-A28 models. Besides that, it is also observed that N_2O and NO masses estimated using SGA-A33 show the same trend in terms of temporal pattern, although there are minor discrepancies in terms of absolute values. The SGA-A28 model also reproduces the in-cylinder averaged temperature as that of its skeletal counterpart in the LGIA simulation. The comparison is illustrated in Figure 9.

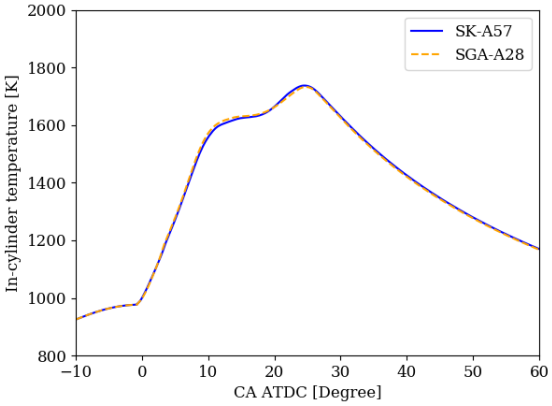

Figure 9. Comparison of in-cylinder average temperature using the SK-A57 and SGA-A28 models.

3 MODEL EVALUATION BASED ON HEAT TRANSFER TO IN-CYLINDER COMPONENTS

3.1 Engine combustion simulation

Following the evaluation of the SGA concept in prediction of combustion and emission characteristics, the SGA model is next applied to study the heat transfer phenomena in a 95 cm bore

LGIM engine and a 60 cm bore LGIA engine. All CFD simulations, i.e., in-nozzle simulation during injection, open-cycle (from exhaust valve open (EVO) to -10 CAD ATDC) and closed-cycle simulations (from -10 CAD ATDC to EVO) are consistently carried out using Simcenter STAR-CCM+ to facilitate the CFD-FEM coupling in Section 4. The in-nozzle and scavenging flow simulations will be introduced in Section 4, while this section describes the closed-cycle, engine combustion simulations.

3.1.1 Initial and boundary conditions

The closed-cycle simulations are set to begin at -10 CAD ATDC. The initial thermochemical conditions are based on an in-house 0D engine simulator, CycSim and are listed in Table 3. Similar to the practice in Section 2, the initial turbulent kinetic energy and the associated dissipation rate are estimated based on swirl number, engine bore size, and engine speed. The initial velocity is represented by a solid-body rotation, where the magnitude of the flow field is obtained from a scavenging flow simulation (see Section 4). Discharge coefficients of each fuel nozzle are estimated based on their respective in-nozzle simulations. The values are used to calculate the rate of injection profiles and are subsequently applied in the spray model setup.

Table 3. Initial thermodynamic and engine operating conditions for 95 cm bore LGIM and 60 cm bore LGIA engine cases.

	LGIM	LGIA
Bore (m)	0.95	0.60
Stroke (m)	3.46	2.40
Engine speed (rev/min)	74	84
$P_{\text{-10 CAD ATDC}}$ (bar)	119	118
$T_{\text{-10 CAD ATDC}}$ (K)	825	832

3.1.2 CFD model setup

The base mesh size is set to approximately 2.5 times the fuel oil nozzle size in both the LGIM and LGIA simulations. Taking advantage of the symmetric positioning of the three fuel oil injectors together with their corresponding LGI injectors, only one-third of the cylinder is simulated (see the top image of Figure 10). The geometry of the LGIM and LGIA injectors are taken into account so that the heat transfer coefficients can be directly exported to the FEM analysis for the computation of the nozzle wall temperature. Figure 10 also illustrates the mesh near the LGIM injector.

The fuel spray, flow, and combustion processes are modelled using the Eulerian-Lagrangian approach. The Huh atomisation model is applied for the primary atomisation, while the Reitz-Diwakar model is used to simulate the secondary fuel droplet break-up. The default Huh Gosman model constant is used, and the mean velocity is an average of the entire rate of injection profile. The break-up model constant, C_{s2} of the Reitz Diwakar model, is calibrated to replicate the experimental HRR. The gas phase is described in the Eulerian framework using URANS in engine combustion simulations, and employing Realisable k-ε model with Two-Layer All y+ Wall Treatment. Redlich-Kwong is implemented as the real gas model. A well-stirred reactor model is used in all simulations, implying that the sub-grid interaction between turbulence and chemistry is not considered. The SGA and skeletal models described in the previous section are compared here. It should be highlighted that radiation is not considered.

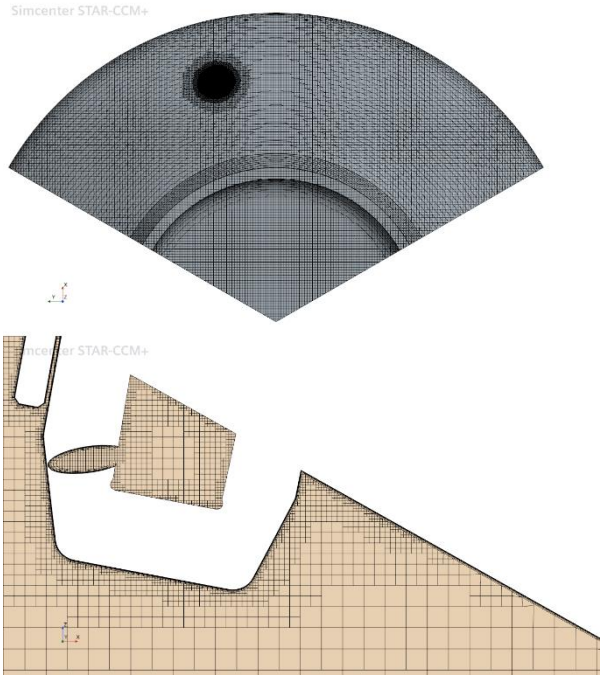

Figure 10. Computational domain used in the LGIM engine combustion simulation.

The temporal terms are discretised using a first-order scheme, while the momentum, mass, and energy equations are spatially discretised with second-order schemes in all simulations. An adaptive time-step setup with mean and maximum CFL numbers of 5 and 50, respectively, is employed. To perform heat transfer calculations, the wall y+ has to be reasonably resolved. In the current engine combustion simulations, a prism layer configuration is customised such that the y+ of all walls remain below 150. This can be seen in Figure 11.

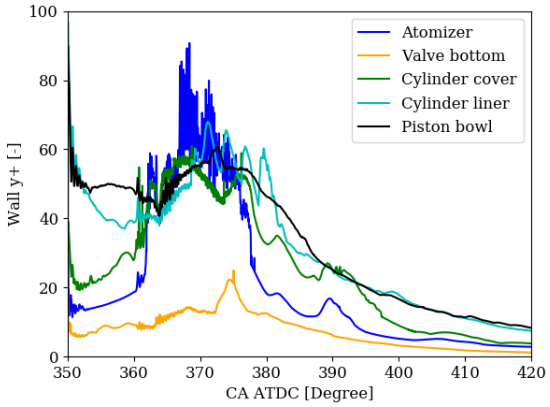

Figure 11. Comparisons of maximum wall y+ for all component walls in the 95 cm bore LGIM simulation.

3.2 Results and discussion

3.2.1 Simulation of 95 cm bore LGIM engine

Both SGA and skeletal models predicted identical combustion starts as well as the location and magnitude of the peak in-cylinder pressure. It should be noted that both models predicted identical average in-cylinder temperatures.

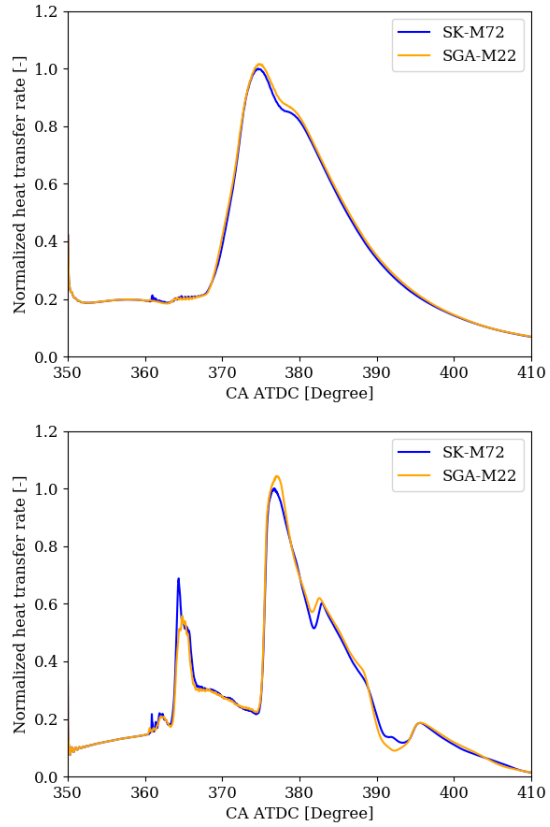

Figure 12. Comparison of normalised heat transfer rates to the piston bowl (top) and methanol injector wall (bottom) in the 95 cm bore LGIM engine simulation using SK-M72 and SGA-M22.

This observation remains the same for the heat transfer to different components when using both the chemistry schemes. Here, only the heat transfer rates on the piston bowl surfaces are presented and shown in Figure 12 for illustration.

Figure 12 also demonstrates that the injector wall experiences the first peak heat transfer shortly after TDC when the pilot fuel combustion reaches the LGIM injector. The heat transfer rate drops until 375 CAD ATDC, and subsequently increases to form a second peak when the jet flame from the neighbouring LGIM injector reaches the injector wall. Spikes appear thereafter, but the magnitudes are less apparent as the overall in-cylinder temperature drops.

3.2.2 Simulation of 60 cm bore LGIA engine

Similar to the 95 cm bore LGIM engine simulation, the onset of the combustion, the location and magnitude of the peak in-cylinder pressure as well as the averaged temperature predicted by the SGA and skeletal models are identical. This observation remains the same for the heat transfer rates to different components.

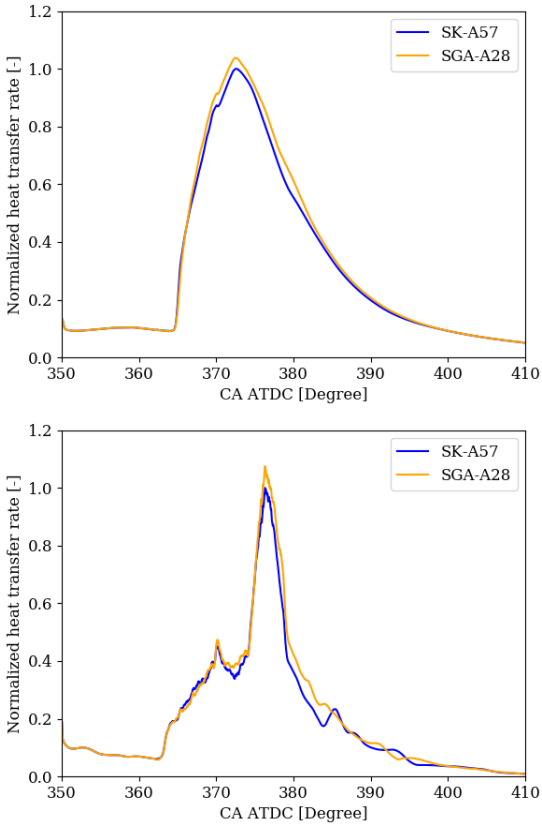

Figure 13. Comparison of normalised heat transfer rates to the piston bowl (top) and ammonia injector wall (bottom) in the 60 cm bore LGIA engine simulation using SK-A57 and SGA-A28.

Figure 13 also demonstrates that the LGIA injector wall experiences the high heat transfer from the pilot fuel combustion after TDC. The heat transfer rate gradually increases, and a small spike is observed at 370 CAD ATDC. The heat transfer rate peaks at 378 CAD ATDC when the jet flame from the upstream LGIA injector arrives. Spikes appear thereafter, but the magnitudes are less apparent. These trends are reasonably well replicated by the SGA-A28 model, despite utilising a simplified chemical mechanism.

4 ESTIMATION OF NOZZLE WALL TEMPERATURE

For a comparison with the temperature measurement, it is not sufficient to compute the injector wall temperature solely from the results of the CFD engine combustion simulation. CFD in-nozzle simulation and scavenging flow simulations must also be carried out. Multiple sets of CFD results, i.e., heat transfer coefficients as well as thermodynamic and flow data at selected locations during an engine cycle, are required by the FEM analysis of injectors:

- in-nozzle heat transfer coefficients during fuel injection
- heat transfer coefficients on nozzle external wall surface during fuel injection
- heat transfer coefficients on nozzle external wall surface before and after fuel injection
- local pressure, temperature, and velocity at a selected point (this will henceforth be known as point data) near the nozzle location for a full engine cycle.

The following sections elaborate the initial/boundary conditions and model setup of the CFD in-nozzle simulation, CFD scavenging flow simulation and FEM. The 95 cm bore LGIM engine presented in Section 3 is simulated in the following sections.

4.1 In-nozzle flow simulation

4.1.1 Initial and boundary conditions

In-nozzle URANS CFD calculations are performed to predict the heat transfer on the internal walls of the injector during the quasi-steady part of the fuel injection. The injection pressure and backpressure are set to 540 bar and 187 bar (compression pressure), respectively. Non-isothermal fluid properties are imported as thermodynamic tables based on the National Institute of Standards and Technology (NIST) database [15]. For internal wall temperatures, multiple iterative simulations of conjugate heat transfer are necessary. An educated guess was made for the wall temperature profile in the first iteration. As depicted in Figure 14, the temperature profile for the internal walls was divided into three regions; a constant temperature of 363 K, a linearly increasing temperature from 363 K to 513 K, and an exponentially increasing temperature from 513 K to 543 K.

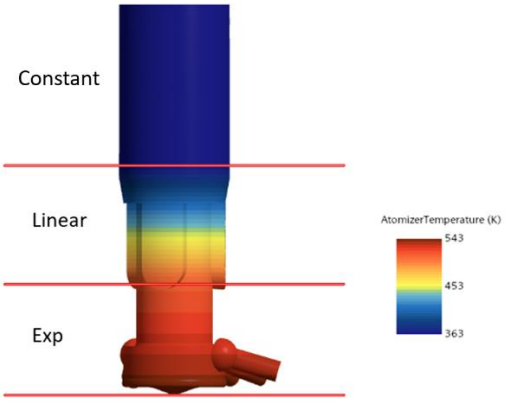

Figure 14. Nozzle wall temperature used in the first iteration of the CFD simulation. ‘Exp’ denotes an exponentially increasing temperature.

4.1.2 CFD model setup

The multiphase flow of fuel liquid and vapour is solved using the volume of fluid method as proposed by Hirt and Nichols [16] coupled with a cavitation model according to Schnerr and Sauer [17]. To ensure realistic upstream flow conditions, the cutoff shaft and spindle guide are included. All geometries are stationary, and the cutoff shaft (needle) is positioned at full lift. The computational domain employed in the internal flow simulations is shown in Figure 15, together with a close-up view of the mesh in a plane section through one of the nozzles.

The region near and in the nozzles, requires the highest degree of refinement to resolve the large gradients in the flow. A mesh size of 0.07 D is used for the core mesh in the holes, where D is the nozzle diameter. The boundary layers are modelled using wall functions, and the wall y+ values are below 150 in the important regions of the domain. The heat transfer coefficients on the internal surfaces of the injector are evaluated at a specified wall y+ of 100, and then exported to the FEM model.

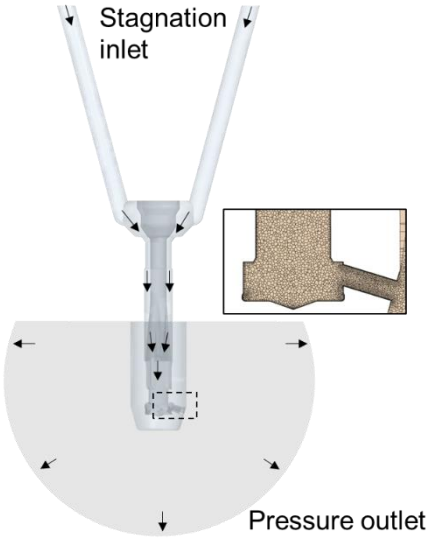

Figure 15. The computational domain used in the in-nozzle flow simulation and a close-up view of the mesh in a cross-sectional plane through one of the nozzles.

4.2 Scavenging flow simulation

4.2.1 Initial and boundary conditions

The open-cycle simulation is performed next, starting from EVO, followed by the blow down, scavenging and push phases. The simulation continues until -10 CAD ATDC, where the closed-cycle CFD engine combustion simulations begin. As mentioned earlier, the initial and boundary conditions of the open-cycle are set according to those provided by the associated CycSim simulation. The initial and boundary thermochemical conditions in each region are provided in Table 4. The initial turbulent intensity, turbulent velocity scale, and turbulent viscosity ratio are set to 0.01, 1 m/s and 10, respectively. Lastly, turbulence intensity and turbulent length scale of both the scavenge box inlet and exhaust bend outlet boundaries are set to 0.01 and 0.01 m, respectively.

Table 4. Initial thermochemical conditions in the 95-cm bore LGIM case.

Region	P (bar)	T (K)	CO_2	H_2O	N_2	O_2
Scavenge box inlet	3.9	307	0.0004	0.008	0.762	0.229
Engine cylinder	7.4	966	0.1060	0.091	0.704	0.010
Exhaust bend outlet	3.7	600	0.0004	0.004	0.765	0.231

4.2.2 CFD model setup

Figure 16 illustrates the computational domain used in scavenging flow simulations. The curtain interface is used for the exhaust valve opening and closure. The interface between the scavenge ports and cylinder is also simulated between intake port open (IPO) and intake port closure (IPC). The mesh sizes are different in various parts of the domain. Inside the cylinder, the mesh size is 0.025 B (B is the cylinder bore) and is set to 0.00625 B around the scavenging ports. In order to accommodate the high-speed flow near EVO and exhaust valve close (EVC), the mesh size is set to less than 0.003125 B in the exhaust valve gap. It should be noted that the current mesh configuration is selected to achieve a compromise between computational efficiency and accuracy in terms of flow prediction.

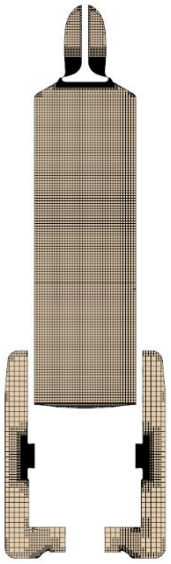

Figure 16. A cross-sectional view of the computational domain used in the scavenging flow simulation.

The Redlich-Kwong real gas model is implemented. Four chemical species of CO_2, H_2O, O_2 and N_2, with temperature-dependent heat capacities are used. Similar to the closed-cycle simulations, URANS is implemented for turbulence modelling, where the Realisable k-ε model with Two-Layer All y+ Wall Treatment is employed. The temporal terms in the URANS equations are discretised using a first-order scheme, while the momentum, mass, and energy equations in the present simulations are spatially discretised with a second-order scheme. The time step size is set to 0.005 CAD. The maximum in-cylinder Convective Courant number remains below 8.0, apart from the first phase of the simulation close to EVO. The scavenge box region is removed after intake port closure and the removal of the exhaust bend region

is performed after EVC to minimise the computational time.

4.3 FEM thermal analysis

The FEM thermal analysis is carried out in ABAQUS as a non-coupled transient heat transfer analysis to simulate the injector temperature throughout the entire engine cycle. To achieve cyclic temperature convergence multiple cycles must be simulated, typically requiring more than 200 cycles. The structural analysis is performed separately, applying the transient temperature field in multiple static steps along with mechanical loading. The outcome is static stress fields for the entire engine cycle, which are then used for a high-cycle fatigue analysis.

4.3.1 Initial and boundary conditions

As described earlier, heat loads during the engine combustion phase (-10 CAD ATDC to EVO) are mapped from the closed-cycle CFD simulation onto the FEM mesh, providing distributed heat transfer coefficients and fluid temperatures on the injector external wall surfaces. The heat loads are updated once every two CADs throughout this phase of the engine cycle.

Similarly, heat loads for the remaining part of the engine cycle are mapped from the open-cycle CFD simulation, ensuring continuous thermal boundary condition coverage over the entire engine cycle. This approach is hereafter referred to as the full cycle-mapped method. To avoid performing the computationally costly open-cycle simulation for any new injector geometry, an in-house point-data scaling methodology is evaluated here. This method is validated by comparing to the temperature predicted using the conventional full cycle-mapped method.

Considering that the cooling effect is similar for all fuel injectors during the scavenging flow process for the same engine and operating conditions, boundary conditions can therefore be provided by a single open-cycle simulation. This approach saves the need for repeated computationally costly open-cycle simulations. The point-data scaling method uses transient data from a single point from the open-cycle simulation to scale the distributed heat load obtained from the closed-cycle simulation. The point location is selected to ensure that the data remains independent of the injector geometry. The spatially distributed heat loads mapped from the closed-cycle simulation at EVO are used for scaling in the interval from EVO to bottom dead centre (BDC). The heat loads from the closed-cycle simulation at -10CAD ATDC are used for scaling in the interval from BDC to -10CAD ATDC. The heat transfer coefficients for the two sets of distributed loads are scaled with λ_{EVO} and $\lambda_{-10\ CAD,}$ respectively. These are described by Eqs. (1) and (2):

$$\lambda_{EVO}(\theta) = \frac{h_{theoretical}(\theta,T(\theta),P(\theta),V(\theta))}{h_{theoretical}(EVO,T(EVO),P(EVO),V(EVO))} \quad (1)$$

$$\lambda_{-10\ CAD}(\theta) = \frac{h_{theoretical}(\theta,T(\theta),P(\theta),V(\theta))}{h_{theoretical}(-10,T(-10),P(-10),V(-10))} \quad (2)$$

where *T*, *P*, and *V* represent temperature, pressure, and velocity, respectively, at a selected point probe near the injector, while $h_{theoretcial}$ is the heat transfer coefficient computed using the averaged Nusselt number for turbulent flow over a flat plate as shown in Eq. (3):

$$\mathrm{Nu} = 0.037 \cdot Re^{4/5} Pr^{1/3} \quad (3)$$

where *Re* is the Reynolds number and *Pr* represents the Prandlt number [18]. Similar to the heat transfer coefficients, the fluid temperature is scaled directly using the temperature at a selected point probe near the injector:

$$\kappa_{EVO}(\theta) = \frac{T(\theta)}{T(EVO)} \quad (4)$$

$$\kappa_{-10CAD}(\theta) = \frac{T(\theta)}{T(-10)} \quad (5)$$

Transient heat loads on the external walls of the injector during the scavenging phase of the engine cycle can then be computed using the scaling functions defined in Eqs. (1), (2), (4) and (5).

Heat loads from the in-nozzle simulation are mapped onto the FEM mesh internal surface elements, providing the distributed heat transfer coefficients and sink temperatures from the methanol flow. The heat loads are applied during the injection period of the engine cycle. A second iteration has been performed, using nodal temperatures as boundary condition for the in-nozzle simulation. Only the injector is included in the FEM model. The heat transfer on the internal part of the cutoff shaft from the in-nozzle CFD simulation is directly mapped to the closest internal surfaces of the injector in the FEM model. The internal cooling occurs mainly near the hole inlets, and hence the effect of excluding the cutoff shaft in the FEM model is considered minimal. The nodal temperature at the cover interface is set to a fixed value based on measurements from previous engines. No boundary condition is applied to the injector/valve interface. The boundary condition at the opposite end of the nozzle tip has, in general, a limited effect on the simulated nozzle tip temperature, which is in focus.

4.3.2 FEM model setup

The average mesh size is set to 2 mm, approximately 2.5% of the external circumference. The mesh has been refined in certain areas of interest, to resolve the distributed heat loads sufficiently and to increase the accuracy of the temperature field, as illustrated in Figure 17. At the injector holes, the mesh size is reduced to 1% of the hole circumference. The mesh has also been refined at the external tip surface. To reduce computational costs, the simulation is run with first-order elements until cyclic convergence is achieved. The final temperature field is then used as the initial condition for a new simulation with second-order elements. A first-order mesh is implemented. The rapidly changing temperature field is most accurately described using second-order elements with a consistent mass matrix. This is in contrast to first-order elements where the heat capacity terms are lumped at the nodes, which can lead to inaccuracies, especially for small time increments. ABAQUS provides a guideline for the relationship between element size and time increment, as described by Eq. (6). If time increments are too small, attention must be paid to potential spurious oscillations in the temperature field:

$$\Delta t > \frac{\rho c}{6k} \Delta l^2 \qquad (6)$$

where ρ is the density, c is the heat capacity, k is the thermal conductivity, and Δl is the element length. The relationship is material-dependent. The guideline is adhered to in the areas with rapidly changing temperatures, where the mesh has been refined. However, in the upper part of the injector, where the temperature field is steadier, the guideline is not followed to reduce runtime.

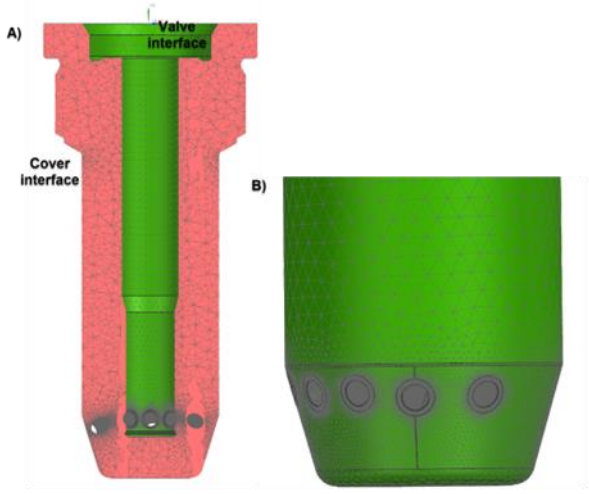

Figure 17. Second-order FEM mesh of the 95 cm bore LGIM injector A) internal structure and B) external wall.

4.4 Results and discussion

4.4.1 In-nozzle flow

The internal cooling of the injector during injection is analysed in the following. All results are evaluated after the second iteration of conjugate heat transfer. The dimensionless Nusselt number, which is the ratio of total heat transfer to conductive heat transfer at wall boundaries, is given as $Nu = hD/k$, where h is the convective heat transfer coefficient, D is the nozzle diameter, and k is the thermal conductivity of the fluid (liquid methanol). Nu distribution is shown in Figure 18 (bottom).

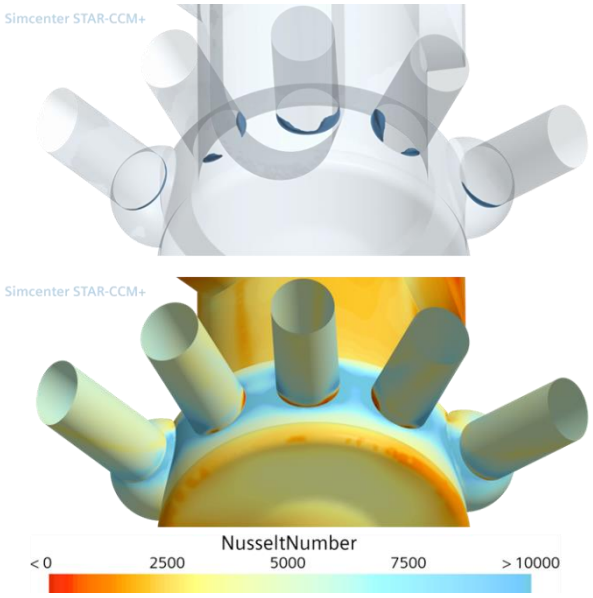

Figure 18. Top: 10% isosurface of vapour volume fraction. Bottom: Nusselt number from in-nozzle CFD calculation.

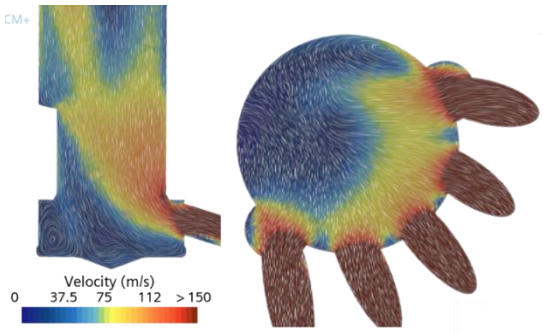

Figure 19. Velocity field in a vertical plane through the centre nozzle (left), and in a horizontal plan in the sac-volume through all nozzles (right).

The most significant cooling occurs between the nozzles where the flow is stagnating, as depicted by the velocity field in Figure 19. It is furthermore seen that the Nusselt number is low in regions with cavitation due to the lower thermal conductivity,

specific heat, and density of methanol vapour relative to liquid (cf. Figure 18). However, the abrupt change in heat transfer near the cavitation area may contribute to local thermal stresses.

4.4.2 Scavenging flow

Similar to the conventional two-stroke marine engines, the in-cylinder flow field is dominated by a wake-like profile, where the introduced scavenge air is concentrated along the liner wall instead of the centre axis. The wall jet structure is caused by a strong vortex, with possible vortex breakdown, located in the centre of the cylinder (not shown). A comparison of in-cylinder pressure during both open and closed cycles can be found in Figure 20. The measured in-cylinder pressure agrees well with those predicted by CycSim and CFD. Besides that, Figure 21 shows that the in-cylinder temperature predicted by CFD agrees with the CycSim results. The scavenging flow simulation results, along with those of the in-nozzle and engine combustion simulations are used to predict the injector temperature in the following section.

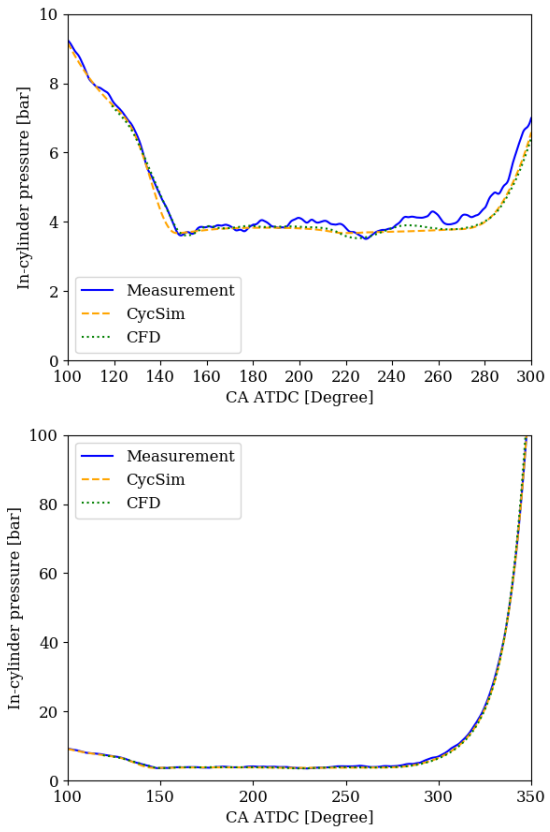

Figure 20. Comparison of in-cylinder pressure from EVO to EVC (top), and from EVC to near TDC (bottom) predicted by CycSim and CFD against the measured pressure.

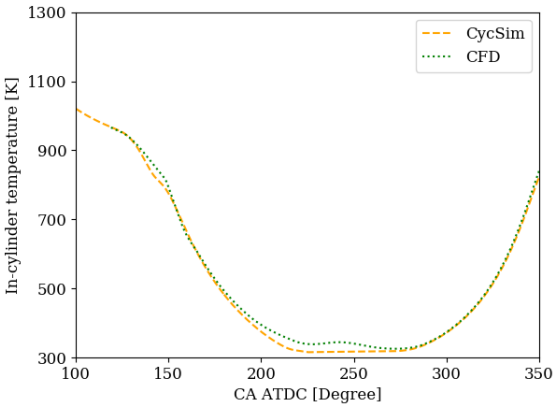

Figure 21. Comparison of in-cylinder temperature from EVO to near TDC predicted by CycSim and CFD.

4.4.3 Comparison of simulated LGIM injector temperature with measurements

The injector temperature was measured at three distinct locations within the injector during a shop test. Standard grounded Ø1.2 mm type-K thermocouples were used for the measurements, mounted with thermal paste to ensure reliable thermal contact. Two thermocouples were positioned 0.6 mm below the external surface at the nozzle tip: one at the swirl stagnation line (FO, front outer) and the other on the swirl lee side (BO, back outer). The third thermocouple was placed near the interface between the injector and the cylinder cover (SO, seat outer). The difference between cyclic average temperatures obtained from measurements and simulations is presented in Figure 22. All the values are normalised using the FO temperature measurement in the diesel model, i.e. FO (D).

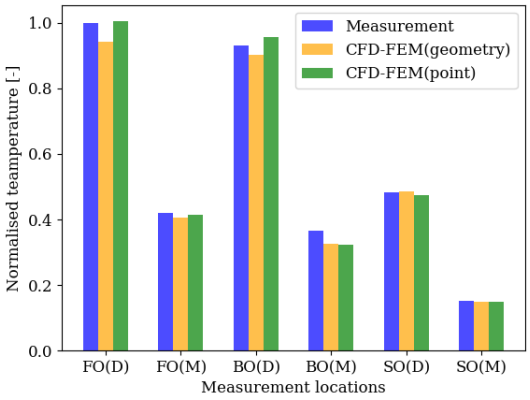

Figure 22. Comparison of CFD-FEM results using geometry and point mapping against methanol injector temperature measurements at different positions for both diesel and LGIM mode. All the values are normalised using the FO temperature measurement in the diesel model, i.e. FO (D).

Figure 22 also demonstrates the performance of the current CFD-FEM coupling toolbox in predicting the injector temperature of the geometry and point mapping modes. The same procedures have been implemented to simulate the diesel mode, where a 32-species mechanism is used [19]. Both approaches correctly predicted the change of temperature with respect to position and operating mode. As compared to the measurement, the maximum percentage difference is approximately 6% for all the simulation results, apart from those for BO in the LGIM mode which is approximately 13%.

5 CONCLUSIONS

The former 50 cm bore LGIM engine simulations [2] are revisited in this work. With the implementation of the CCM-P2P solver, the LGIM simulations show a 3-fold speed-up compared to the former CCM version. In addition, the CCM-P2P solver is applied to simulate a 50 cm bore LGIA engine. By considering additional principal variables of NO and N_2O, the CCM-P2P solver reproduces the results from the direct integration (without clustering method) reasonably well. The speed-up may reach up to 75%, depending on the chemical mechanism size. It should be mentioned that the speed-up gained in the LGIA simulation is lower than that in the LGIM simulation. This is mainly due to the higher number of CCM phase-space cells required to accommodate the more complex ammonia chemistry.

The SGA concept is also evaluated for the LGIA combustion simulation. Two SGA models and a skeletal mechanism are used. During the main combustion and post-oxidation phases, the evolutions of NH_3, NH_2 and OH predicted by all models are identical. High levels of agreement for the temporal evolutions of N_2O and NO masses between the SK-A57 and SGA-A28 models are observed. Those estimated using SGA-A33 show the same trend in terms of temporal pattern, although there are minor discrepancies in terms of absolute values. The SGA-A28 model also reproduces the in-cylinder averaged temperature as that of its skeletal counterpart in the LGIA simulation. Such a speed-up allows the implementation of more comprehensive chemical mechanisms, providing more insights into the in-cylinder processes and facilitating evaluation of different chemical mechanisms' performance.

Further appraisal is made in terms of predicting heat transfer to different engine components during the engine combustion phase for a 95 cm bore LGIM engine and a 60 cm bore LGIA engine. The SGA models are able to reproduce the temporal evolution of heat transfer to different engine components, including those to the external wall of fuel injectors.

Section 4 of the paper presents the integrated CFD-FEM toolbox for the estimation of the external injector wall temperature. Such evaluation is carried out for the 95 cm bore LGIM engine. Two operating modes are simulated, i.e., diesel mode and methanol mode. The full cycle in-cylinder pressure predicted by the current CFD model is first compared with the measurement from the engine shop test. A comparison of the integrated CFD-FEM results against the external injector wall temperature measurements shows that the current model can replicate the measurements reasonably well. The CFD-FEM toolbox is able to predict the temperature change with respect to measurement positions and operating modes correctly. As compared to the measurement, the maximum percentage difference is approximately 6% for all the simulation results, apart from those for the back outer position in the LGIM mode, which is approximately 13%. Once further validated, such a toolbox will be useful for the injector layout.

6 ACKNOWLEDGEMENTS

The authors acknowledge that their contribution is part of the project ENGIMMONIA that has received funding from the European Research Council (ERC) under the European Union's Horizon 2020 research and innovation program (Grant agreement No. 955413), and the project AEngine funded by Innovationsfonden Danmark. Nicolai Quist acknowledges Innovationsfonden Danmark for partially financing his industrial PhD. The authors would like to thank Professor Xue-Song Bai and Yuchen Zhou from Lund University for sharing the CCM-P2P code and valuable inputs.

7 REFERENCES AND BIBLIOGRAPHY

[1] Mayer, S., Kaltoft, J., Christensen, H., Cong, S., Hult, J., Pang, K.M., Svensson, J. and Sjöholm, J. 2023. Developing the MAN B&W dual fuel ammonia engine. CIMAC Congress Paper no. 589, Busan, South Korea.

[2] Pang, K.M., Sjöholm, J., Xu, S., Bai, X.-S., Hashemi, H., Glarborg, P. and Mayer, S. 2023. Modelling of dual-fuel combustion in a large two-stroke engine using an advanced CFD-chemical model. CIMAC Congress Paper no. 106, Busan, South Korea.

[3] Jangi, M. and Bai, X.-S. 2012. Multidimensional chemistry coordinate mapping approach for combustion modeling with finite-rate chemistry. Combustion Theory and Modelling, 16: 1109-1132.

[4] Anon. The OpenFOAM Foundation. Accessible in 2023.

[5] Müller, U.C., Peters, N. and Liñán, A. 1992. Global kinetics for *n*-heptane ignition at high pressures. Symposium (International) on Combustion, 24(1): 777-784.

[6] Thorsen, L., Nordhjort, C., Hashemi, H., Pang, K.M. and Glarborg, P. 2021. Evaluation of a semiglobal approach for modeling methane/*n*-heptane dual-fuel ignition, Energy & Fuels, 35(17): 14042-14050.

[7] Anon. ANSYS Chemkin Pro. Accessible in 2023.

[8] Lu, T. and Law, C.K. 2008. Strategies for mechanism reduction for large hydrocarbon: *n*-heptane. Combustion and Flame, 154:153-163.

[9] Alekseev, V.A and Nilsson, E.J.K. 2024. Reduced kinetics of NH_3/*n*-heptane: Model analysis and a new small mechanism for engine applications, Fuel, 367: 131464.

[10] Wang, B., Dong, S., Jiang, Z., Gao, W., Wang, Z., Li, J., Yang, C., Wang, Z. and Cheng, X. 2023. Development of a reduced chemical mechanism for ammonia/*n*-heptane blends. Fuel, 338: 127358.

[11] Chang, Y., Jia, M., Wang, P., Niu, B. and Liu, J. 2022. Construction and derivation of a series of skeletal chemical mechanisms for n-alkanes with uniform and decoupling structure based on reaction rate rules. Combustion and Flame, 236: 111785.

[12] Thorsen, L.S., Jensen, M.S.T., Pullich, M.S., Christensen, J.M., Hashemi, H., Glarborg, P., Alekseev, V.A., Nilsson, E.J., Wang, Z., Mei, B. and Liu, N. 2023. High pressure oxidation of NH_3/*n*-heptane mixtures. Combustion and Flame, 254: 112785.

[13] Pichler, C. 2020. Identification of principal chemical subsets of biofuel combustion: Ants walking in renewable fire. PhD thesis. Lund University, Lund, Sweden.

[14] Stagni, A. Cavalotti, C., Arunthanayothin, S., Song, Y. Herbinet, O., Battin-Leclerc, F. and Faravelli, T. 2020. An experimental, theoretical and kinetic-modeling study of the gas-phase oxidation of ammonia. Reaction Chemistry & Engineering, 5: 696-711.

[15] Lemmon E.W., Huber M.L., McLinden M.O. 2018. National Institute of Standards and Technology (NIST). Standard Reference Database 23: Reference Fluid Thermodynamic and Transport Properties - REFPROP, Version 10.0, Available: https://www.nist.gov/srd/refprop.

[16] Hirt C.W. and Nichols B.D. 1981. Volume of Fluid (VOF) method for the dynamics of free boundaries. Journal of Computational Physics, 39(1), 201–225.

[17] Sauer J. and Schnerr G.H. 2000. Unsteady cavitating flow - a new cavitation model based on a modified front capturing method and bubble dynamics, American Society of Mechanical Engineers, Fluids Engineering Division.

[18] Incropera, F.P., DeWitt, D.P., Bergman, T.L. and Lavine, A.S. (2007). Fundamentals of Heat and Mass Transfer (6th ed.). John Wiley & Sons.number

[19] Pang, K.M., Karvounis, N., Walther, J.H. and Schramm, J. 2016. Numerical investigation of soot formation and oxidation processes under large two-stroke marine diesel engine-like conditions using integrated CFD-chemical kinetics. Applied Energy, 169: 874-887.

8 CONTACT

Kar Mun Pang
Senior Research Engineer, Ph.D.

MAN Energy Solutions
Research and Development Two-stroke
Teglholmsgade 41
2450 Copenhagen SV
Denmark

Phone: +45 33 85 11 00 (reception)
Phone: +45 33 85 13 05 (direct)
Fax: +45 33 85 10 30 (fax)
Email: Kar.Pang@man-es.com